Journal of Materials Chemistry A

ROYAL SOCIETY OF CHEMISTRY

PAPER

View Article Online
View Journal | View Issue

Cite this: J. Mater. Chem. A, 2024, 12, 475

Rational design of a carbon/potassium poly(heptazine imide) heterojunction for enhanced photocatalytic H_2 and H_2O_2 evolution†

Christian Mark Pelicano, *[a] Jiaxin Li,[a] María Cabrero-Antonino,[b] Ingrid F. Silva,[a] Lu Peng,[a] Nadezda V. Tarakina,[a] Sergio Navalón,[b] Hermenegildo García[b] and Markus Antonietti *[a]

We present the rational design of carbon/potassium poly(heptazine imide) (KPHI) heterostructures *via* one-step salt-melt assisted condensation for efficient photocatalysis. Hybridizing KPHI with an adenine-derived carbonaceous material (Ad-carbon) displayed an outstanding photocatalytic H_2 evolution activity (738 μmol h^{-1} g_{cat}^{-1}; with 3 wt% Pt as the cocatalyst) and photocatalytic H_2O_2 production (3.94 mmol h^{-1} g_{cat}^{-1}). We establish that the Ad-carbon simultaneously operates as an electron acceptor and a photosensitizer based on structural, optical and photo(electro)chemical characterization. Building an intimate heterojunction between the Ad-carbon and KPHI induced spatial charge separation and prolonged the carrier lifetime. From electrocatalysis, we confirmed that coupling Ad-carbon with KPHI enhanced the surface reaction kinetics towards H_2 evolution and O_2 reduction reactions. Moreover, visual evidence of superior charge transport in the hybrid photocatalyst is revealed through the photodeposition of smaller Pt nanoparticles (~7 nm) with uniform distribution on the carbon regions, which also accounts for the increased catalytic activity.

Received 20th September 2023
Accepted 24th November 2023

DOI: 10.1039/d3ta05701a

rsc.li/materials-a

1 Introduction

With ever-increasing energy demand and global environmental crises, substantial efforts have been devoted to replacing conventional fuels with carbon-neutral energy sources. Even though storage of hydrogen (H_2) gas is a technological challenge in the shift towards a decarbonized economy, H_2 is considered an essential renewable energy carrier and reactant for CO_2 reduction.[1,2] Likewise, hydrogen peroxide (H_2O_2) is another promising green energy carrier (60 wt% aqueous H_2O_2 has a similar energy density (3.0 MJ l^{-1}) to that of H_2 compressed at 35 MPa (2.8 MJ l^{-1}))[3] and a valuable oxidizing agent for disinfection and in organic chemistry.[4] However, the conventional production routes, such as steam reforming for H_2 and the anthraquinone process for H_2O_2, require an extensive amount of fossil energy.[5,6] Eco-friendly and energy-efficient production processes for H_2 and H_2O_2 are therefore still welcome.

Solar-driven photocatalysis using particulate semiconductors is a promising paradigm towards sustainable production of valuable chemical fuels.[7,8] Poly(heptazine imide), a new type of highly crystalline carbon nitride, has already stood out among emerging photocatalysts owing to its non-toxic nature, extreme stability, visible-light absorption and suitable energy-level positions that meet the requirements for H_2 and H_2O_2 evolution.[9,10] Remarkable milestones in maximizing solar-conversion efficiencies of carbon nitrides include a number of effective strategies such as nanostructuring, reducing the stacking distance, defect engineering and introduction of donor–acceptor functionalities.[11–14] Apart from these methods, constructing heterojunctions is a longstanding tool to boost the photoactivity by driving photoexcited electrons and holes toward opposite directions owing to the presence of a built-in electric field. In turn, this enhanced charge separation allows more carriers to facilitate the desired redox reactions.[15]

In general, carbonaceous materials (CMs) in photocatalysis can serve as modifiers on the surface of semiconductors or as photosensitizers themselves.[16–20] Recent advances have demonstrated that π-conjugated bonding between g-C_3N_4 and CMs (*e.g.*, graphene, carbon dots and carbon nanotubes) can create an intimate electronic contact and promote charge transport from the light transducer to the carbon surface, thus preventing carrier recombination.[21–23] CMs can also extend the light absorption and take on the role of a photosensitizer.[24,25] In view of these promising properties, constructing carbon/poly(heptazine imide) hybrid photocatalysts is promising for sustainable H_2 and H_2O_2 production. This has to be

[a]Department of Colloid Chemistry, Max Planck Institute of Colloids and Interfaces, Potsdam 14476, Germany. E-mail: christianmark.pelicano@mpikg.mpg.de; markus.antonietti@mpikg.mpg.de

[b]Departamento de Química, Instituto de Tecnología Química (CSIC-UPV), Universitat Politècnica de València, València 46022, Spain

† Electronic supplementary information (ESI) available. See DOI: https://doi.org/10.1039/d3ta05701a

accompanied by determining the governing principles for the interaction of CMs with carbon nitride, which is of great importance in developing visible-light responsive photocatalysts. In this work, we hybridize an adenine-derived porous carbon (Ad-carbon) with potassium poly(heptazine imide) (KPHI) *via* salt melt-assisted condensation for photocatalytic H_2 and H_2O_2 evolution. An extensive analysis using optical and photo(electro)chemical characterization along with microscopy enabled a comprehensive look into the photocatalytic enhancement mechanism within the hybrid material.

2 Results and discussion

2.1 Physicochemical characterization of CM and CM/KPHI

Three different types of pre-synthesized carbonaceous materials (CMs) were used as KPHI modifiers. A nitrogen-doped, porous carbon (Ad-carbon) was synthesized from adenine and cesium acetate based on a salt-melt templating route reported by our group.[26] Secondly, carbon dots (CDs) were prepared *via* a microwave-assisted reaction of citric acid and urea. As a final choice, 4-hydroxy-1*H*-pyrrolo[3,4-*c*]pyridine-1,3,6(2*H*,5*H*)-trione (HPPT-carbon) was made by heating a solvent-free mixture of citric acid and urea (please see the ESI for a detailed preparation route for all the carbons†).[27] Fig. S1A† shows the X-ray diffraction (XRD) patterns of the CMs. Ad-carbon shows a small diffraction peak at 26.4° and high-intensity sloping at lower angles, suggesting poor graphitic stacking and the presence of micropores, respectively.[28] A broad diffraction peak at 26° can be seen in the XRD pattern of the CDs which implies poor crystallinity.[27] In contrast, HPPT-carbon exhibited a rather narrow diffraction peak at 27°, indicating a higher degree of graphitization than the two other samples. As expected, the Fourier transform infrared (FTIR) spectra of HPPT-carbon and CDs show almost identical vibrational modes (Fig. S1B†), which is in agreement with earlier reports on citric acid/urea derived carbons.[29] No characteristic absorption bands are detected for Ad-carbon due to the decomposition of functional groups during its high-temperature carbonization (800 °C). Scanning electron microscopy (SEM) images show a stark difference between the morphologies of CM samples, as shown in Fig. S2.† It can be observed that the Ad-carbon has a three-dimensional hierarchical macroporous structure owing to the presence of salt templates (Fig. S2A and Table S1†). A closer inspection reveals that its rough surface is further composed of smaller pores resulting in a high specific surface area of above >3000 m^2 g^{-1}. On the other hand, CDs and HPPT display comparable high-density bulk structures possessing a low surface area of ~1.2–1.5 m^2 g^{-1} (Fig. S2C and D†).

The overall synthetic process to hybridize carbonaceous structures into the KPHI matrix is illustrated in Fig. 1A. According to the type of CM added to KPHI (CM = Ad, CD, HPPT), the samples are denoted as CM/KPHI. To fabricate the hybrids, CMs were ground with 5-aminotetrazole and KCl/LiCl salt eutectic by ball milling. These mixtures were then heated in N_2 flow at 600 °C for 4 h to obtain yellowish-brown powder samples (see the ESI for a detailed synthesis protocol†). The preparation for pure KPHI follows the same protocol but without CMs. First, comprehensive characterization techniques were carried out to examine the chemical structure and composition of the CM/KPHI series.

Based on the XRD patterns of the hybrids (Fig. 1B), all of them show the characteristic diffraction peaks of KPHI. More specifically, the diffraction peak at 28° corresponds to the interplanar stacking of layers while the peak at 8° can be ascribed to the periodicity of heptazine units within the layers.[30] Fig. 1C shows that the hybrids possess similar functional groups as pristine KPHI. The sharp band at 801 cm^{-1} is assigned to the heptazine ring out-of-plane bending mode whereas the intense absorption bands in the range of 1200–1650 cm^{-1} are typically associated with the stretching modes of the heptazine heterocyclic ring. Additionally, the peaks at 2140 and 2180 cm^{-1} are a result of unreacted cyano groups while broad bands between 3000 and 3700 cm^{-1} signify the presence of N–H and O–H bonds.[31] The preservation of the chemical structure of KPHI indicates that the CMs did not modify the KPHI framework. UV-vis diffuse reflectance spectroscopy (DRS) further verified the integration of the carbons with KPHI, in which a slight enhancement in light absorption is evident (Fig. 1D). The structural changes upon hybrid formation were followed by SEM (Fig. S3†). The pure KPHI sample features micron-sized assemblies of rod-like nanocrystals. Apparently, KPHI modified with CMs revealed very similar morphologies except for HPPT/KPHI which shows severe agglomeration of much larger nanorods. From bulk elemental analysis, all the hybrids have an estimated C/N ratio of 0.62, further verifying their chemical similarity and excluding the formation of other carbon nitride phases (Table S2†). The addition of various CMs during the condensation of KPHI resulted in a comparable surface area and average pore size between the hybrids (Table S1 and Fig. S4†). This finding suggests that these properties should not be a deciding factor in their overall photocatalytic activities.

2.2 Photocatalytic H_2 and H_2O_2 evolution performance

The photocatalytic performance of the as-synthesized catalysts was first evaluated by the H_2 evolution reaction using triethanolamine (10 v/v% TEOA) as a hole scavenger under white LED illumination (λ > 420 nm). All the photocatalyst systems were nominally deposited with 3 wt% Pt. As illustrated in Fig. 2A, only the KPHI modified with microwave-synthesized CDs displayed a lower activity (295 μmol h^{-1} g^{-1}) than pristine KPHI (453 μmol h^{-1} g^{-1}). It is well-known that along with its hole-accepting nature, CDs show a strong affinity for H_2O molecules.[27] This partially inhibits the oxidation of TEOA by the photogenerated holes and increases charge recombination, thereby reducing the overall photocatalytic activity of the CD/KPHI system. Interestingly, hybridizing KPHI with other carbon materials enhances the H_2 evolution production. In particular, the Ad/KPHI hybrid exhibits the highest average H_2 evolution rate of 663 μmol h^{-1} g^{-1} among all the studied catalysts; which is 50% and 25% higher than that of the parental KPHI (453 μmol h^{-1} g^{-1}) and HPPT/KPHI (525 μmol h^{-1} g^{-1}). The calculated apparent quantum yield (AQY) for Ad/KPHI is

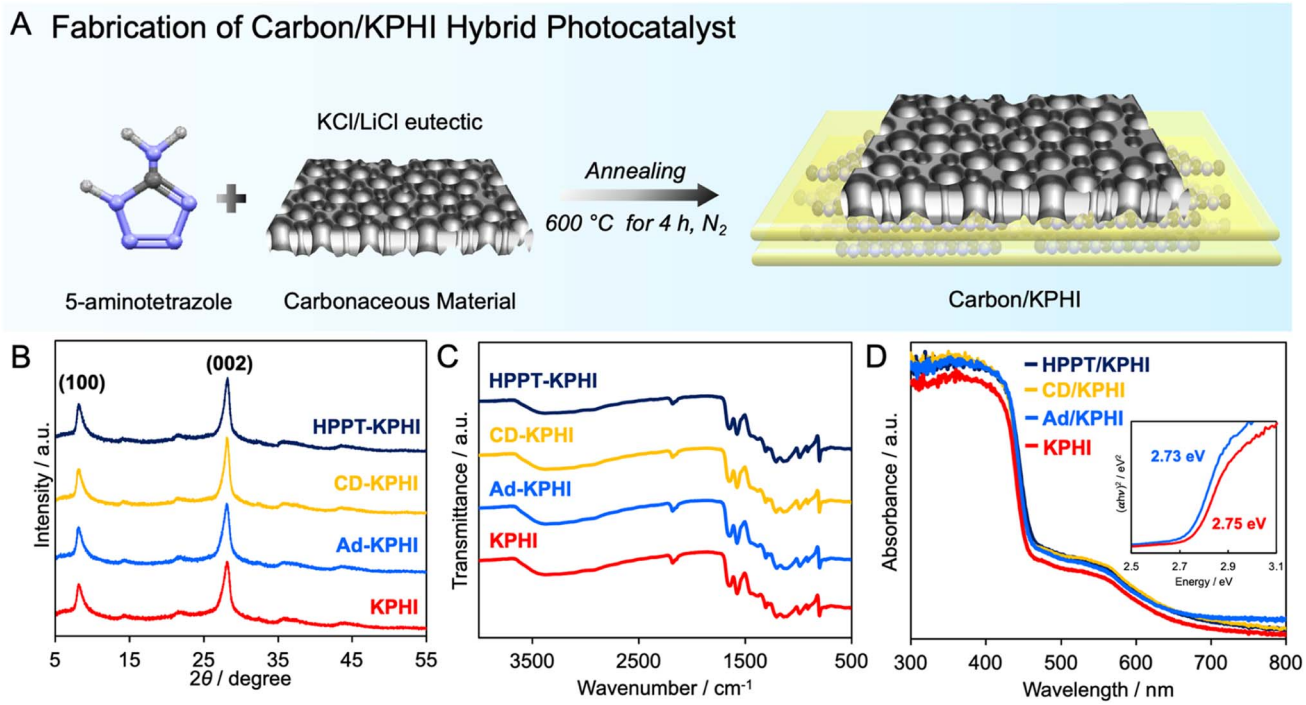

Fig. 1 (A) Schematic diagram for preparing CM/KPHI hybrid photocatalysts. (B) XRD patterns, (C) FTIR spectra and (D) UV-vis DRS spectra of various CM/KPHI hybrids (inset: the Tauc plot of KPHI and Ad/KPHI).

5.8% at 410 nm excitation wavelength (*vs.* 3.6% for KPHI). Notably, Ad/KPHI reached a maximum H_2 evolution rate of 738 μmol h^{-1} g^{-1}, which is much higher than most reported values for carbon nitrides (Table S3†). No H_2 is detected for pure KPHI and Ad/KPHI without Pt, excluding the possibility of carbon functioning as a cocatalyst for H_2 evolution (Fig. S5†). Taking

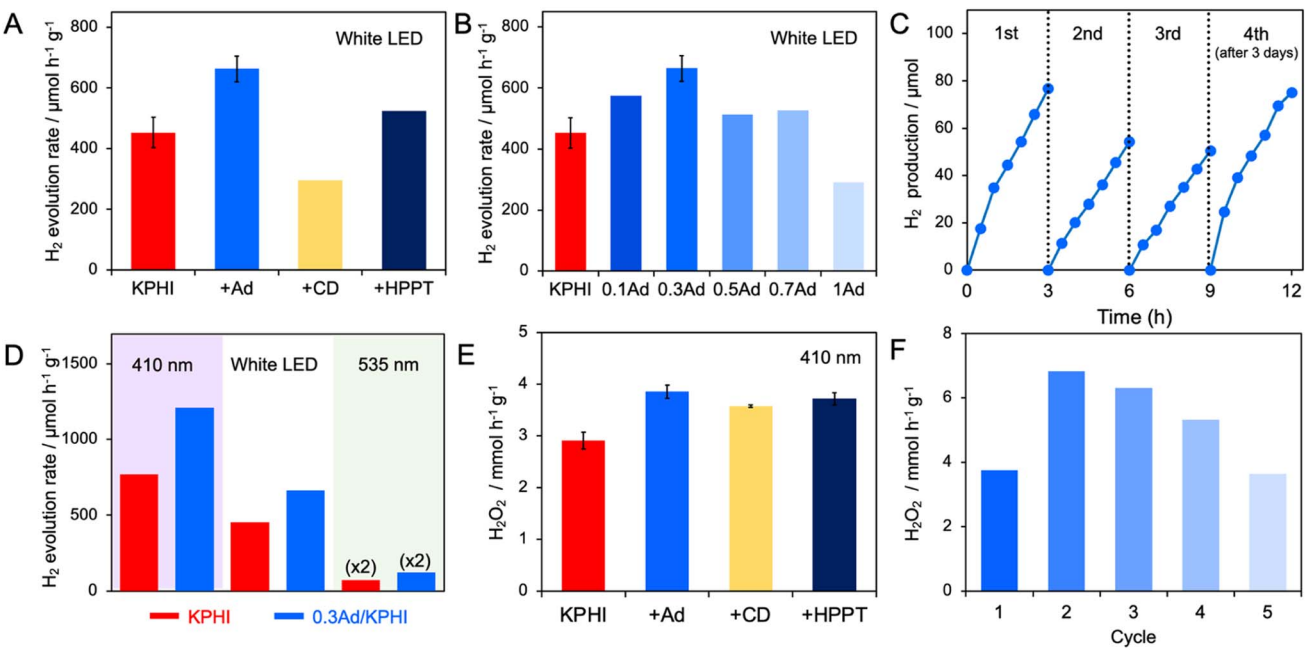

Fig. 2 (A) Photocatalytic H_2 evolution rates of KPHI and CM/KPHI hybrids. (B) Influence of Ad-carbon loading on the H_2 evolution performance of KPHI. (C) Recyclability tests for 0.3Ad/KPHI in the H_2 evolution reaction. (D) H_2 evolution rates of KPHI and 0.3Ad/KPHI using different excitation wavelengths. Reaction conditions: photocatalyst, 50 mg; solvent, 38 ml H_2O (10 vol% TEOA); 3 wt% Pt cocatalyst. (E) Photocatalytic H_2O_2 production activities of KPHI and CM/KPHI hybrids. (F) Recyclability tests for 0.3Ad/KPHI in H_2O_2 production. Reaction conditions: photocatalyst, 5 mg; solvent, 2 ml of 3.5% w/w glycerin bubbled with O_2 for 1 min before the reaction; light source, violet LED ($\lambda = 410$ nm).

into account that a simple mixture of Ad-carbon with pure KPHI displayed a much lower activity (319 μmol h^{-1} g^{-1}, Fig. S5†), our findings clearly establish a distinct synergy in the Ad-carbon/KPHI-heterostructure in enhancing the HER activity.

The optimal amount of Ad-carbon loading is 0.3 mg (denoted as 0.3Ad/KPHI) *vs.* 1 g of 5-aminotetrazole, possibly, to reach a suitable balance between light absorption and the number of active sites (Fig. 2B). Increasing the Ad-carbon concentration to more than 0.3 mg did not induce any structural damage to KPHI (Fig. S6†) but reduced its photoactivity. The decrease in activity is possibly attributed to the light-shielding effect of the excess carbon on the surface of KPHI. To assess the recyclability of 0.3Ad/KPHI, consecutive runs were carried out using the same set-up and experimental conditions (Fig. 2C). The reaction was allowed to continue over the span of 12 h with intermittent degassing of the reactor every 3 h. A slight decrease in the initial evolution rate is ascribed to the strong adsorption of oxidation products of TEOA on the photocatalyst surface, which prevents the interaction of fresh TEOA with the active sites. This trend is in agreement with the previous reports that employed TEOA as a sacrificial electron donor.[32,33] Note that the photodeposition of Pt greatly affects the first cycle. Nevertheless, no evident structural change occurred in the optimized photocatalyst as indicated by its corresponding XRD and FTIR spectra before and after recyclability tests (Fig. S7†).

In addition, 0.3Ad/KPHI maintained its H_2 evolution activity without any sign of serious degradation under continuous irradiation over a span of 20 h, demonstrating the robust nature of the catalyst (Fig. S8†). These results highlight the excellent durability of 0.3Ad/KPHI for sustainable solar-driven H_2 production. To elucidate the relationship between the photocatalytic activity and light absorption, the influence of excitation wavelength on H_2 evolution activity was analyzed, as shown in Fig. 2D. When the system was irradiated with a violet LED (λ = 410 nm), 0.3Ad/KPHI presented a 55% increase in the H_2 evolution rate in comparison to KPHI. Remarkably, the optimized material is still active even at an excitation wavelength of 535 nm. Even though the activity at higher excitation wavelength is lower due to the missing bandgap absorption mode in KPHI, a larger increase of 75% in the performance with respect to KPHI is still observed.

In order to verify if the coupling between KPHI and carbonaceous materials can also realize a performance breakthrough for H_2O_2 production, we performed sacrificial photocatalytic H_2O_2 evolution with O_2-saturated glycerin aqueous solution (3.5 v/v%), with the glycerin also working as a hole scavenger under 410 nm LED irradiation. All the samples were used without any metal cocatalysts (*e.g.*, Pt metal group and Ag) since they are known to catalytically decompose H_2O_2.[10] As shown in Fig. 2E, all the CM/KPHI hybrids exhibited higher H_2O_2 production rates compared with pure KPHI, indicating once again the crucial role of heterojunctions for improving catalytic activity. Likewise, 0.3Ad/KPHI produced the largest amount of H_2O_2 (0.0197 mmol h^{-1}), which is 30% higher than that of pure KPHI (0.0151 mmol h^{-1}) and among the best production rates reported in the literature (Table S4†). 0.3Ad/KPHI has an AQY value of 1.1% at 410 nm, which is slightly higher than that of pure KPHI (0.94%). The low AQY values could be associated with inadequate reactor design and the use of a high-intensity LED irradiation source.[10] Aside from photocatalytic activity, the recycling stability of 0.3Ad/KPHI was also examined (Fig. 2F). After 5 consecutive cycles, 97% of the original activity was retained which further validates its excellent stability. Surprisingly, a 1.8-fold activity enhancement after the 1st cycle occurred for 0.3Ad/KPHI. Separate studies comparably described a stronger catalytic performance upon catalyst recycling for Na-PHI, H-PHI and W-doped TiO_2 photocatalysts.[10,34] However, after repeated tests, the color of the optimized sample changed from yellowish-brown to grayish-white powder, indicating a structural or chemical change in the hybrid catalyst. Fig. S9A† shows a shift in the diffraction peak from 28° to 27.6°, indicating a change in the interlayer π–π stacking of the heptazine rings. Based on the FTIR spectra of the recycled hybrid catalyst, new bands emerged at 3254 and 2869 cm^{-1} which are related to the presence of –NH and –CH groups, respectively (Fig. S9B†). Furthermore, the band attributed to metal–nitrogen stretching (M–NC_2) disappeared. These changes possibly indicate that some protons from the sacrificial reagent (glycerin) reacted with the anionic sites on the surface of the photocatalyst, which is in agreement with our previous work.[10] Integrating porous carbon with KPHI creates additional traps for the protons and most importantly accelerates carrier transport, resulting in the best photocatalytic H_2O_2 performance reported so far. Not only this, we assume that a pre-protonated 0.3Ad/KPHI hybrid variant could reach higher activities since more protons are now available for the O_2 reduction reaction. In fact, the higher H_2O_2 yield after the first cycle partly confirms this hypothesis (Fig. 2F).

2.3 Optical, photo(electro)chemical and structural characterization

To unravel the enhanced photocatalytic activity occurring over 0.3Ad/KPHI, we performed comprehensive optoelectronic, electrochemical and structural characterization. The band structures of photocatalysts are the main indicators of their capability to drive redox reactions and their charge separation efficiencies. On this premise, the optical properties and band diagram of 0.3Ad/KPHI were first investigated. As stated earlier, integrating KPHI with 0.3Ad extended its light absorption and at the same time slightly narrowed its bandgap (2.75 eV for KPHI and 2.73 eV for 0.3Ad/KPHI) (Fig. 1D, inset). Based on Mott–Schottky analysis (Fig. S10†), the introduction of Ad-carbon shifted the flat-band potential (E_{fb}) of KPHI anodically from −0.12 eV to −0.07 eV (*vs.* RHE) while it had a little effect on the valence band maximum (roughly 2.65 eV, Fig. 3A). Thermodynamically, the conduction band position corresponds to E_{fb}, and a positive shift in the conduction band suggests a lower energy barrier, which is beneficial for the maximum utilization of photoexcited electrons in reducing H^+ and O_2 to H_2 and H_2O_2, respectively.[35] Moreover, the Mott–Schottky plot of 0.3Ad/KPHI displays a smaller slope than that of KPHI, further confirming that 0.3Ad/KPHI has a higher charge carrier density. As supporting observations, a previous study has fairly established

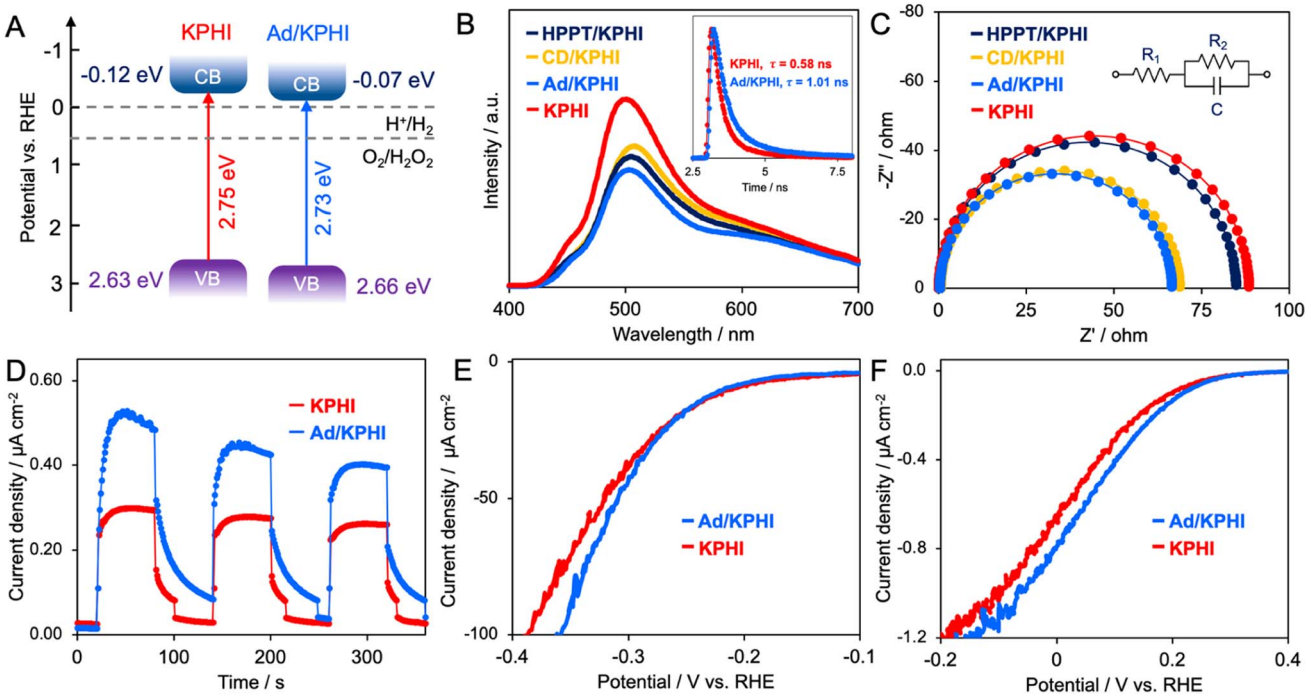

Fig. 3 (A) Experimentally determined band structures of KPHI and 0.3Ad/KPHI. (B) Room temperature steady-state PL emission spectra of KPHI and CM/KPHI hybrids with an excitation wavelength of $\lambda = 360$ nm (inset: solid-state time-resolved PL decay of KPHI and 0.3Ad/KPHI). (C) Electrochemical impedance spectroscopy (EIS) Nyquist plots and (D) transient photocurrent ($\lambda > 420$ nm, applied potential 0.3 V) for KPHI and 0.3Ad/KPHI in 0.2 M Na_2SO_4 aqueous solution. LSV curves of KPHI and the 0.3Ad/KPHI hybrid in N_2- and O_2-saturated 0.2 M Na_2SO_4 aqueous solutions to evaluate their (E) HER and (F) ORR electrocatalytic activities, respectively.

that the incorporation of a carbon ring in g-C_3N_4 (C_{ring}–C_3N_4 heterostructure) caused an accumulation of free electrons around the Fermi level leading to an increase in H_2O adsorption energy and reduction of the energy barrier for intermediate formation during photocatalytic reactions.[36] Another density functional theory calculation revealed that additional energy states appeared around the Fermi level of a carbon-modified graphitic carbon nitride. Consequently, the existence of such states boosts the direct transfer of electrons at equal potential based on the polaron hopping mechanism.[37]

The charge separation efficiency over the KPHI and hybrid samples was monitored by steady-state photoluminescence (PL) spectroscopy (Fig. 3B). Upon excitation at 360 nm, all the hybrids showed an identical emission shape ranging from 400 to 700 nm with a maximum at 500 nm, which originates from the radiative recombination of photogenerated charge carriers. The modification of KPHI with Ad-carbon quenched its PL emission the most, demonstrating the effective suppression of radiative electron–hole recombination and faster charge separation at the Ad-carbon/KPHI heterojunction interface. As shown in the inset of Fig. 3B, the solid-state time-resolved fluorescence decay spectra show that the presence of Ad-carbon prolongs the average carrier lifetime from 0.58 ns (pristine KPHI) to 1.01 ns (0.3Ad/KPHI). Normally, an extended lifetime denotes a higher probability for the charge carriers to react with reactive substrates and initiate the intended photocatalytic reactions. To gain a better insight on the differences in photocatalytic behavior between pure KPHI and 0.3Ad/KPHI, PL lifetime measurements were carried out under different experimental conditions in aqueous suspensions, *i.e.*, in the presence of hole scavengers (TEOA and glycerine) and with or without deposited Pt (Fig. S11†). The overall lifetimes of 0.3Ad/KPHI are lower compared with those of KPHI under all conditions indicating a more efficient usage of photogenerated electrons for H^+ and O_2 reduction reactions (Table S5†). More specifically, the addition of hole scavengers and the Pt cocatalyst reduced the τ_{ave} values, which suggests faster electron transfer from the hybrid photocatalyst to the adsorbed reactant species.[38]

Electrochemical impedance spectroscopy (EIS) measurements were performed at 0 V *vs.* the Ag/AgCl electrode to further investigate the charge transfer at different CM–KPHI interfaces. The Nyquist plots were fitted according to a modified Randle circuit (Fig. 3C, inset), where R_1, R_2, and C are the electrolyte resistance, charge transfer resistance, and constant phase element for the electrolyte and electrode interface, respectively.[39] A smaller diameter of the semicircle in a Nyquist plot represents a lower value for R_2 and a higher carrier transfer efficiency. As revealed in Fig. 3C, 0.3Ad/KPHI shows the smallest semicircle, which verifies the elevated conductivity of the hybrid and partially explains its superior photocatalytic activity among the samples. This result is consistent with the transient photocurrent response (TPR) measurements performed at 0.3 V *vs.* the reference electrode under white LED irradiation ($\lambda > 420$ nm). Fig. 3D shows that the optimized hybrid produces a photocurrent of ~0.53 μA cm^{-2}, approximately 75% higher than that of pure KPHI (0.3 μA cm^{-2}) which implies that the

charge transfer is essentially promoted. Another compelling phenomenon comes from the slightly delayed photocurrent response of the 0.3Ad/KPHI hybrid compared with KPHI during the "on–off" irradiation cycles. A slower increase in the photocurrent response upon irradiation signifies that the photogenerated electrons can be captured and stored by the Ad-carbon, after which just a fraction of the electrons is transferred to the FTO electrode until an equilibrium state is attained. Furthermore, an incremental release of electrons from Ad-carbon could trigger a slower response as indicated by a delay curve when the irradiation is turned off. A similar behavior has been reported wherein photoexcited electrons were stored within the carbon sites at the interface of Au nanocrystals and TiO_2 particles.[40] Taken together, these observations strongly indicate that at higher excitation energies (410 nm and white LED), Ad-carbon primarily serves as an electron sink to extract the photogenerated electrons from the conduction band of KPHI, thus facilitating more efficient carrier separation (Fig. S12†). To address the question of the possible minor contribution of Ad-carbon as a photosensitizer, TPR measurements were conducted under green and red LED irradiation. Fig. S13† shows that a 1.9- and 1.3-fold increase in photocurrent values are recorded for 0.3Ad/KPHI relative to pristine KPHI when illuminated with green and red LEDs, respectively. Given these considerable boosts in photocurrent responses (*vs.* white LED excitation, a 0.75-fold increase), it is logical to assume that the Ad-carbon also acts as a photosensitizer on top of its main role as an electron acceptor. Apparently, the contribution of Ad-carbon as the photosensitizer becomes more obvious at lower excitation energies. This is proven by the absence of a delayed response in the TPR curves of the hybrid sample (Fig. S13†). Nonetheless, it should be pointed out that the role of Ad-carbon as a potential source of electrons is restricted by its small quantity within the hybrid (Fig. S12†). Besides, the surface reaction kinetics occurring over KPHI and 0.3Ad/KPHI hybrid systems were evaluated by linear sweep voltammetry (LSV). The electrocatalytic H_2 evolution and O_2 reduction activities are measured in N_2- and O_2-saturated 0.2 M Na_2SO_4 aqueous solution, respectively (Fig. 3E and F). Notably, larger cathodic currents are observed for the 0.3Ad/KPHI hybrid at the same potential window with respect to KPHI, indicating that the incorporation of Ad-carbon accelerates the H^+ and O_2 reduction kinetics on the photocatalyst surface, which supports our photocatalysis results.

To provide a visual illustration of the improved rate of charge transport induced by the hybridization of Ad-carbon with KPHI, the location and distribution of photodeposited Pt nanoparticles across the hybrid surface were examined using transmission electron microscopy (TEM). The TEM image of Ad-carbon highlights typical amorphous flakes with the absence of any long-range order within the material (Fig. 4A),[41] while that of KPHI is composed primarily of crystalline aggregates (Fig. 4B). Analysis of the HRTEM images and the corresponding FFTs suggests that the particles crystallize in a hexagonal structure with unit cell parameters $a = 12.6$ Å and $c = 3.3$ Å.[42] A representative HAADF-STEM image of 3Ad/KPHI (Fig. 4C) and its corresponding secondary electron TEM image (Fig. 4C, inset) before the photocatalytic reaction illustrate the complex nature of the samples. The formation of large K-PHI agglomerates suggests that they might have been deposited on some flat surface or contain an additional layered phase from which KPHI crystals nucleated. At the same time, a few big particles of amorphous carbon which are not covered by K-PHI crystals are visible in the sample. After the H_2 evolution reaction (Fig. 4D), considerably fewer amounts of rod-like KPHI nanocrystals are found to be connected to the big amorphous particles. It can be seen that the Pt nanoparticles are located mostly in the amorphous regions. Similar observations from other randomly selected areas likewise verify that most of the Pt nanoparticles are preferentially deposited on the porous Ad-carbon (Fig. S14†). Fig. 4E and S15A† show that the photodeposition of Pt on pure KPHI resulted in the growth of large and agglomerated Pt particles (23.6 ± 9.3 nm). On the other hand, smaller Pt nanoparticles with an average diameter of 7.4 ±

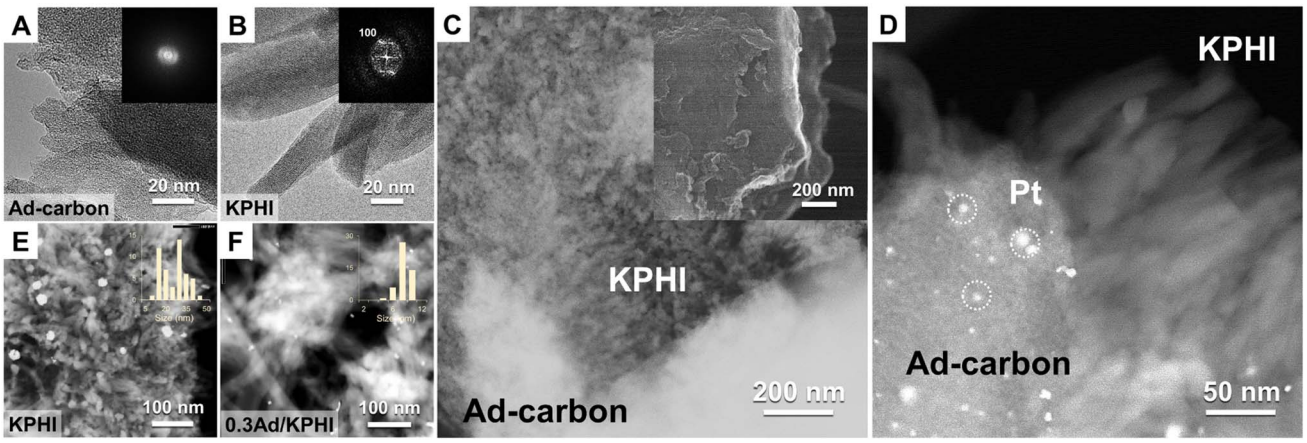

Fig. 4 TEM images of (A) Ad-carbon and (B) KPHI. High angle annular dark-field (HAADF)-STEM images of 3Ad/KPHI (C) before and (D) after 6 h of the H_2 evolution reaction. (In order to locate the Ad-carbon/KPHI heterojunction more easily during STEM observation, we prepared a hybrid sample with 10× the concentration of 0.3Ad/KPHI.) HAADF-STEM images of (E) KPHI and (F) 0.3Ad/KPHI with photodeposited Pt nanoparticles.

1.5 nm are found to be homogeneously distributed across the hybrid photocatalyst surface (Fig. 4F and S15B†), which is supported by energy-dispersive X-ray spectroscopy (EDS) elemental mapping images (Fig. S15C†). The reduction in size of the photodeposited Pt nanoparticles implies an increase in the number of electron pathways or reductive sites and provides strong chemical evidence of the effective suppression of carrier recombination.

3 Conclusion

In summary, we presented a strategic design of nanocarbon–KPHI heterostructures to improve both spectral coverage and separation of the photogenerated charges while facilitating electron transfer over the materials interfaces. Three different carbons (CD, Ad-carbon and HPPT) were explored to form heterojunctions with KPHI. Our results identified that the CD was not a suitable modifier, while the Ad-carbon and HPPT showed appropriate conductivities and band alignment with KPHI, resulting in an enhanced photoactivity. The optimal Ad-carbon/KPHI hybrid unveiled a remarkable photocatalytic H_2 evolution activity (738 μmol h^{-1} $g_{cat}{}^{-1}$) and H_2O_2 production (3.94 mmol h^{-1} $g_{cat}{}^{-1}$), demonstrating the synergistic effect between KPHI and Ad-carbon in augmenting photocatalytic performance. Photo(electro)chemical measurements revealed that Ad-carbon mainly functions as an electron sink and concurrently as a photosensitizer when coupled with KPHI. The addition of Ad-carbon stabilized the electrons and accelerated the reduction reaction kinetics on the surface of the hybrid photocatalyst. STEM images indicate that smaller Pt nanoparticles created by photoreduction mostly deposit in the amorphous carbon-rich regions, which provides solid chemical evidence of the electron-accepting characteristic of the carbon and the faster interfacial charge transfer. These findings establish the governing principles for the enhancement mechanism occurring over carbon/carbon nitride heterostructures and offer general design guidelines for the next generation of high-performance carbon–nitrogen based photocatalysts for solar energy conversion.

Conflicts of interest

There are no conflicts of interest to declare.

Acknowledgements

The authors gratefully acknowledge Bolortuya Badamdorj for the SEM and TEM measurements, Antje Völkel for measuring elemental analysis, Jessica Brandt for ICP-OES measurements, Ursula Lubahn for technical support, and Volker Strauss for the synthesis of HPPT-carbon. We acknowledge the financial support of the Max Planck Society. I. F. S. thanks the Alexander von Humboldt Foundation for her postdoctoral fellowship. S. N. acknowledges the support of Grant PID2021-123856OBI00 funded by MCIN/AEI/10.13039/501100011033 and by ERDFA way of making Europe. Open Access funding was provided by the Max Planck Society.

References

1 M. Saruyama, C. M. Pelicano and T. Teranishi, *Chem. Sci.*, 2022, **13**, 2824–2840.
2 I. F. Teixeira, N. V. Tarakina, I. F. Silva, N. López-Salas, A. Savateev and M. Antonietti, *Adv. Sustainable Syst.*, 2022, **6**, 2100429.
3 K. Mase, M. Yoneda, Y. Yamada and S. Fukuzumi, *Nat. Commun.*, 2016, **7**, 11470.
4 Z. Tian, Q. Zhang, L. Thomsen, N. Gao, J. Pan, R. Daiyan, J. Yun, J. Brandt, N. López-Salas, F. Lai, Q. Li, T. Liu, R. Amal, X. Lu and M. Antonietti, *Angew. Chem., Int. Ed.*, 2022, **61**, 202206915.
5 W. Liu, P. F. Wang, J. Chen, X. Gao, H. N. Che, B. Liu and Y. H. Ao, *Adv. Funct. Mater.*, 2022, 2205119.
6 G. Z. S. Ling, S. F. Ng and W. J. Ong, *Adv. Funct. Mater.*, 2022, **32**, 2111875.
7 C. M. Pelicano, M. Saruyama, R. Takahata, R. Sato, Y. Kitahama, H. Matsuzaki, T. Yamada, T. Hisatomi, K. Domen and T. Teranishi, *Adv. Funct. Mater.*, 2022, **32**, 2202987.
8 C. M. Pelicano and H. Tong, *Appl. Res.*, 2023, e202300080, DOI: 10.1002/appl.202300080.
9 A. Galushchinskiy, C. Pulignani, H. Szalad, E. Reisner, J. Albero, N. V. Tarakina, C. M. Pelicano, H. García, O. Savateev and M. Antonietti, *Sol. RRL*, 2023, **7**, 2300077.
10 A. Rogolino, I. F. Silva, N. Tarakina, M. A. R. da Silva, G. F. S. R. Rocha, M. Antonietti and I. F. Teixeira, *ACS Appl. Mater. Interfaces*, 2022, **14**(44), 49820–49829.
11 H. Ou, P. Yang, L. Lin, M. Anpo and X. Wang, *Angew. Chem., Int. Ed.*, 2017, **56**, 10905–10910.
12 P. Zhang, Y. Tong, Y. Liu, J. J. M. Vequizo, H. Sun, C. Yang, A. Yamakata, F. Fan, W. Lin, X. Wang and W. Choi, *Angew. Chem., Int. Ed.*, 2020, **59**, 16209–16217.
13 G. Zhang, G. Li, Z. A. Lan, L. Lin, A. Savateev, T. Heil, S. Zafeiratos, X. Wang and M. Antonietti, *Angew. Chem., Int. Ed.*, 2017, **129**, 13630–13634.
14 G. Zhang, L. Lin, G. Li, Y. Zhang, A. Savateev, S. Zafeiratos, X. Wang and M. Antonietti, *Angew. Chem.*, 2018, **130**, 9516–9520.
15 Y. Wang, R. Godin, J. R. Durrant and J. Tang, *Angew. Chem.*, 2021, **60**, 20811–20816.
16 M. Odziomek, P. Giusto, J. Kossmann, N. V. Tarakina, J. Heske, S. M. Rivadeneira, W. Keil, C. Schmidt, S. Mazzanti, O. Savateev, L. Perdigón-Toro, D. Neher, T. D. Kühne, M. Antonietti and N. López-Salas, *Adv. Mater.*, 2022, **34**, 2206405.
17 B. Li, W. Peng, J. Zhang, J. C. Lian, T. Huang, N. Cheng, Z. Luo, W. Q. Huang, W. Hu, A. Pan, L. Jiang and G. F. Huang, *Adv. Funct. Mater.*, 2021, **31**, 2100816.
18 G. A. M. Hutton, B. Reuillard, B. C. M. Martindale, C. A. Caputo, C. W. J. Lockwood, J. N. Butt and E. Reisner, *J. Am. Chem. Soc.*, 2016, **138**, 16722–16730.
19 B. Jana, Y. Reva, T. Scharl, V. Strauss, A. Cadranel and D. M. Guldi, *J. Am. Chem. Soc.*, 2021, **143**, 20122.

20 L. Zhao, X. Chen, X. Wang, Y. Zhang, W. Wei, Y. Sun, M. Antonietti and M. M. Titirici, *Adv. Mater.*, 2010, **22**, 3317–3321.
21 M. R. Hoffmann, S. T. Martin, W. Choi and D. W. Bahnemann, *Chem. Rev.*, 1995, **95**, 69–96.
22 X. Huang, X. Qi, F. Boey and H. Zhang, *Chem. Soc. Rev.*, 2012, **41**, 666–686.
23 Y. Jiao, Q. Huang, J. Wang, Z. He and Z. Li, *Appl. Catal., B*, 2019, **247**, 124.
24 S. Bhattacharyya, F. Ehrat, P. Urban, R. Teves, R. Wyrwich, M. Döblinger, J. Feldmann, A. S. Urban and J. K. Stolarczyk, *Nat. Commun.*, 2017, **8**, 1401.
25 S. L. Xie, H. Su, W. J. Wei, M. Y. Li, Y. X. Tong and Z. W. Mao, *J. Mater. Chem. A*, 2014, **2**, 16365–16368.
26 J. Li, J. Kossmann, K. Zeng, K. Zhang, B. Wang, C. Weinberger, M. Antonietti, M. Odziomek and N. López-Salas, *Angew. Chem., Int. Ed.*, 2023, e202217808.
27 Y. Wang, X. Liu, X. Han, R. Godin, J. Chen, W. Zhou, C. Jiang, J. F. Thompson, K. B. Mustafa, S. A. Shevlin, J. R. Durrant, Z. Guo and J. Tang, *Nat. Commun.*, 2020, **11**, 2531.
28 T. Pfaff, F. M. Badaczewski, M. O. Loeh, A. Franz, J. U. Hoffmann, M. Reehuis, W. G. Zeier and B. M. Smarsly, Comparative Microstructural Analysis of Nongraphitic Carbons by Wide-Angle X-Ray and Neutron Scattering, *J. Phys. Chem. C*, 2019, **123**, 20532–20546.
29 J. D. Stachowska, A. Murphy, C. Mellor, D. Fernandes, E. N. Gibbons, M. J. Krysmann, A. Kelarakis, E. Burgaz, J. Moore and S. G. Yeates, *Sci. Rep.*, 2021, **11**, 10554.
30 M. Y. Ye, S. Li, X. J. Zhao, N. V. Tarakina, C. Teutloff, W. Y. Chow, R. Bittl and A. Thomas, *Adv. Mater.*, 2020, **32**, 1903942.
31 J. Zhang, G. Ye, C. Zhang, Z. Pan, S. Wang, G. Zhang and X. Wang, *ChemSusChem*, 2022, **15**, e202201616.
32 D. Dontsova, S. Pronkin, M. Wehle, Z. Chen, C. Fettkenhauer, G. Clavel and M. Antonietti, *Chem. Mater.*, 2015, **27**, 5170–5179.
33 J. Kröger, A. Jiménez-Solano, G. Savasci, P. Rovó, I. Moudrakovski, K. Küster, H. Schlomberg, H. A. Vignolo-González, V. Duppel, L. Grunenberg, C. B. Dayan, M. Sitti, F. Podjaski, C. Ochsenfeld and B. V. Lotsch, *Adv. Energy Mater.*, 2020, **11**, 2003016.
34 K. Sorathiya, B. Mishra, A. Kalarikkal, K. P. Reddy, C. S. Gopinath and D. Khushalani, *Sci. Rep.*, 2016, **6**, 35075.
35 J. Zhang, X. Chen, K. Takanabe, K. Maeda, K. Domen, J. D. Epping, X. Fu, M. Antonietti and X. Wang, *Angew. Chem., Int. Ed.*, 2010, **49**, 441–444.
36 W. Che, W. Cheng, T. Yao, F. Tang, W. Liu, H. Su, Y. Huang, Q. Liu, J. Liu, F. Hu, Z. Pan, Z. Sun and S. Wei, *J. Am. Chem. Soc.*, 2017, **139**, 3021–3026.
37 M. Xiao, Y. Jiao, B. Luo, S. Wang, P. Chen, M. Lyu, A. Du and L. Wang, *Nano Res.*, 2021, **16**, 4539–4545.
38 E. Mitchell, A. Law and R. Godin, *J. Photochem. Photobiol., C*, 2021, **49**, 100453.
39 J. Wang, Y. Fan, R. Pan, Q. Hao, Y. Wu, T. van Ree and R. Holze, *ACS Appl. Energy Mater.*, 2021, **4**(11), 13288–13296.
40 L. Liu, T. D. Dao, R. Kodiyath, Q. Kang, H. Abe, T. Nagao and J. Ye, *Adv. Funct. Mater.*, 2014, **24**, 7754–7762.
41 S. Youk, J. P. Hofmann, B. Badamdorj, A. Völkel, M. Antonietti and M. Oschatz, *J. Mater. Chem. A*, 2020, **8**, 21680–21689.
42 A. Savateev, N. V. Tarakina, V. Strauss, T. Hussain, K. ten Brummelhuis, J. M. Sánchez Vadillo, Y. Markushyna, S. Mazzanti, A. P. Tyutyunnik, R. Walczak, M. Oschatz, D. M. Guldi, A. Karton and M. Antonietti, *Angew. Chem., Int. Ed.*, 2020, **59**, 15061–15068.

